

Image of Kerr-de Sitter black holes illuminated by equatorial thin accretion disks

Ke Wang,¹ Chao-Jun Feng,^{1,*} and Towe Wang^{2,†}

¹*Division of Mathematical and Theoretical Physics,*

Shanghai Normal University, 100 Guilin Road, Shanghai 200234, P.R.China

²*Department of Physics, East China Normal University, Shanghai 200241, China*

To explore the influence of the cosmological constant on black hole images, we have developed a comprehensive analytical method for simulating images of Kerr-de Sitter black holes illuminated by equatorial thin accretion disks. Through the application of explicit equations, we simulate images of Kerr-de Sitter black holes illuminated by both prograde and retrograde accretion disks, examining the impact of the cosmological constant on their characteristic curves, relative sizes, and observed intensities. Our findings reveal that, in comparison to Kerr black holes, the cosmological constant not only diminishes the relative size of a black hole but also amplifies its luminosity. Moreover, an observer's relative position in the universe (r_0/r_C) can influence both the relative size and luminosity of a black hole, where r_0 is the distance from the observer to the black hole, r_C is the cosmological horizon determined by the value of the cosmological constant Λ .

I. INTRODUCTION

In April 2019, the Event Horizon Telescope (EHT) collaboration released images of the core of the galaxy M87 (M87*) based on 1.3mm interferometric observations [1–6]. These images all acknowledge a ring-like structure of typical diameter $\sim 40\mu\text{as}$. This is important evidence of the existence of black holes, and it raises the intriguing prospect of testing general relativity with future high-resolution black hole images.

The basic feature of black hole images is a bright ring surrounding a dark area [7]. Early theoretical studies mainly focused on the central dark area of black hole images [8, 9], commonly regarded as the ‘black hole shadow’. Specifically, in numerous previous studies of black hole shadows [10–34], the black hole shadow corresponds to the geometric shape of the projection of the photon sphere/shell on an observer’s sky, where the photon sphere/shell is a region composed of bound photon orbits. Recently there has been some controversy over the term ‘black hole shadow’ [35, 36]. To avoid inaccuracy of terminology, we use the term ‘critical curve’ introduced by [37] to represent the edge of the black hole shadow. The size and shape of the critical curve can usually be analytically calculated, even for black holes of the Plebanski-Demiński class (Kerr-de Sitter black holes are a special case of this class.) [38–41]. Unlike the critical curve, studying the black hole image mostly requires numerical simulation. The first simulated black hole image presented in [42] displays a Schwarzschild black hole surrounded by a rotating luminous accretion disk. Similar equatorial accretion disk models are now widely used to simulate black hole images and are capable of producing similar results to general-relativistic magnetohydrodynamic (GRMHD) simulations [43–45].

In [46], the authors employ a cutting-edge dictionary-learning-based algorithm named PRIMO, utilizing high-fidelity simulations of accreting black holes as a training set. By discerning correlations among various regions of the interferometric data space, this methodology facilitates the recovery of high-fidelity images, even in scenarios of sparse coverage, enabling attainment of the nominal resolution of the EHT array. In [47], the authors present that the predictive values for massive black holes exhibit universality within a broad class of quantum-modified spacetime, incorporating the scenario of a black hole transitioning to a white hole. Consequently, their findings introduce a new experimental avenue to scrutinize predictions of quantum gravity. In [48], the authors capture the polarized image of a rotating black hole enveloped by a cold dark matter halo. In [49], the author investigates primary images (PIs) and secondary images (SIs) resulting from strong gravitational lensing around a Kerr black hole shadow. In [50], symmergent gravity is evaluated through shadow imaging and weak field photon deflection by a rotating black hole, utilizing results from M87* and Sgr. A*. In [51], the authors test black hole mimickers using the Event Horizon Telescope image of Sagittarius A*. In [52], polarized images of a synchrotron-emitting ring in the spacetime of a rotating black hole within the scalar–tensor–vector–gravity (STVG) theory are explored. In [53], the observational appearance of a Kerr-Melvin black hole (KMBH) illuminated by an accretion disk is studied. In [54], the authors investigate null geodesics of a class of charged, spherical, and asymptotically flat hairy black holes in an Einstein-Maxwell-scalar theory with nonminimal coupling for the scalar and electromagnetic fields. In [55], the Hubble law is extracted through frequency-shift considerations of test particles revolving around the Kerr black hole

* Corresponding author; fengcj@shnu.edu.cn

† twang@phy.ecnu.edu.cn

in asymptotically de Sitter spacetime. In [56], the authors delve into the correspondence between the shape of the shadow and Kerr parameters, extending it to a general rotating black hole generated by the Newman-Janis algorithm, as detailed in Refs. [57] and [58]. The authors investigate images of a reduced Kiselev black hole in [59] and images of nonsingular nonrotating black holes in conformal gravity in [60]. For additional works, refer to the reviews in [61] [62] and also [63].

In principle, a camera aimed at a black hole sees an infinite sequence of self-similar ring-like structures near the critical curve, the ring-like structure in the black hole image is named ‘the photon ring’ [9, 43, 64]. in which subrings arise from photons that differ by the number of half-orbits they complete around the black hole on the way from their source to the detector. These subrings may produce strong and universal signatures on long interferometric baselines [43].

The cosmological constant Λ , as we know, is the simplest model to explain the cosmic accelerating expansion, and the corresponding cosmological model is commonly called the Λ cold dark matter (Λ CDM) model [65]. In a universe with a non-zero cosmological constant Λ , a rotating black holes could be described by the Kerr-de Sitter (KdS) metric discovered by Carter [66], and today we know that it is a special case of the general Plebanski-Demiński family of metrics [38].

Although the current observations of M87* have limited resolution, and it is anticipated that the impact of the cosmological constant on the black hole image will be minimal, it remains crucial to elucidate how the cosmological constant may influence the black hole image. Previous investigations into Kerr-de Sitter black hole shadows have demonstrated that the cosmological constant reduces the size of the critical curve [67, 68]. In this paper, we try to investigate the effects of the cosmological constant on the black hole images and the possibility of using black hole images to test the cosmological constant. We build upon and extend a simple geometric model proposed by [69] in Kerr black hole spacetimes, which was later simplified by [44] and employed to fit the GRMHD results. In this model, the black hole is surrounded by a geometrically and optically thin equatorial accretion disk. Particles in the accretion disk move along time-like geodesics, while the emission profiles remain stationary and axisymmetric. We gradually establish imaging methods suitable for this type of model, including analytical ray tracing methods, and finally make the formula for generating black hole images completely explicit.

This paper is organized as follows: In section II, we review the Kerr-de Sitter spacetime and establish the equatorial disk model. In section III, we describe the complete method of generating images, in which the analytical ray tracing is discussed in section IV. Our results from various simulations are presented in section V. Finally, we summarize our work in section VI.

Throughout the paper we will use geometric units $c = G = 1$ and the convention of metric is $(-, +, +, +)$.

II. SPACETIME OF KERR-DE SITTER BLACK HOLES

In this section, we briefly review the geodesic equations of the Kerr-de Sitter spacetime and the equatorial circular orbits. After that, an analytic accretion disk model will be described. For a more detailed treatment of equatorial circular orbits, refer to [70].

A. The spacetime and geodesics

In standard Boyer-Lindquist coordinates (t, r, θ, ϕ) , the metric of Kerr-de Sitter spacetime [66] is

$$ds^2 = \frac{a^2 \sin^2 \theta \Delta_\theta - \Delta_r}{\Xi^2 \Sigma} dt^2 - 2 \frac{a \sin^2 \theta (\Delta_\theta (a^2 + r^2) - \Delta_r)}{\Xi^2 \Sigma} dt d\phi + \frac{\Sigma}{\Delta_r} dr^2 + \frac{\Sigma}{\Delta_\theta} d\theta^2 + \frac{\sin^2 \theta (\Delta_\theta (a^2 + r^2)^2 - a^2 \Delta_r \sin^2 \theta)}{\Xi^2 \Sigma} d\phi^2, \quad (1)$$

where M, a are the mass and spin of the black hole, $\Lambda > 0$ is the cosmological constant, and

$$\begin{aligned} \Sigma &= r^2 + a^2 \cos^2 \theta, \\ \Delta_r &= (r^2 + a^2) \left(1 - \frac{\Lambda}{3} r^2\right) - 2Mr, \\ \Delta_\theta &= 1 + \frac{\Lambda}{3} a^2 \cos^2 \theta, \\ \Xi &= 1 + \frac{\Lambda}{3} a^2. \end{aligned} \quad (2)$$

In the following, we define a the dimensionless cosmological constant

$$y = \frac{1}{3}\Lambda M^2, \quad (3)$$

then we set $M = 1$, such that the coordinates x^μ , the spin a and the line element ds becomes dimensionless.

According to the symmetry of the spacetime, three geodesic constants can be defined: the total energy E , the axial angular momentum L , and the Carter constant Q [66]. E and L correspond to the Killing vectors ∂_t and ∂_ϕ , respectively, and Q is related to the ‘hidden symmetry’ of spacetime. These three constants, together with the conserved Hamiltonian $H = \mu/2$, simplify the geodesic equation into four first-order differential equations, which can be compactly written as

$$g_{\mu\nu}\dot{x}^\nu = p_\mu = \left(-E, \pm_r \frac{\sqrt{\bar{R}(r)}}{\Delta_r}, \pm_\theta \frac{\sqrt{\bar{\Theta}(\theta)}}{\Delta_\theta}, L \right), \quad (4)$$

where p_μ is the canonical momentum, $\pm_r = \text{sgn}(p^r)$, $\pm_\theta = \text{sign}(p^\theta)$, and we have defined

$$\begin{aligned} \bar{\Theta}(\theta) &= -\Xi^2(L \csc \theta - aE \sin \theta)^2 + (Q + (aE - L)^2 \Xi^2 + \mu(a^2 - a^2 \sin^2 \theta)) \Delta_\theta, \\ \bar{R}(r) &= (a^2 E - aL + Er^2)^2 \Xi^2 - (Q + (aE - L)^2 \Xi^2 - r^2 \mu) \Delta_r. \end{aligned} \quad (5)$$

The null geodesics, $\mu = 0$, is determined only by two parameters $\lambda = L/E$ and $\eta = Q/E^2$ called the impact parameters. So the null geodesics can be recast in the form of

$$g_{\mu\nu}\dot{x}^\nu = p_\mu = E \left(-1, \pm_r \frac{\sqrt{R(r)}}{\Delta_r}, \pm_\theta \frac{\sqrt{\Theta(\theta)}}{\Delta_\theta}, \lambda \right), \quad (6)$$

where

$$\begin{aligned} \Theta(\theta) &= \Delta_\theta (\Xi^2(a - \lambda)^2 + \eta) - \Xi^2(\lambda \csc \theta - a \sin \theta)^2, \\ R(r) &= \Xi^2(a^2 - a\lambda + r^2)^2 - \Delta_r (\Xi^2(\lambda - a)^2 + \eta). \end{aligned} \quad (7)$$

B. Equatorial timelike geodesics

The timelike geodesics on equatorial plane possess conserved quantities $Q = 0$ and $\mu = -1$, then the radius function reduced from Eq. (4) is

$$\Sigma^2 r^2 = (a^2 E - aL + Er^2)^2 \Xi^2 - ((L - aE)^2 \Xi^2 + r^2) \Delta_r \equiv V(r). \quad (8)$$

The equatorial circular orbits require $V(r) = V'(r) = 0$, whose solutions obtained by [70] are

$$E_\pm \Xi = \frac{1 - \frac{2}{r} - (r^2 + a^2)y \pm a \left(\frac{1}{r^3} - y\right)^{1/2}}{\sqrt{1 - \frac{3}{r} - a^2 y \pm 2a \left(\frac{1}{r^3} - y\right)^{1/2}}}, \quad (9)$$

$$L_\pm \Xi = \frac{-2a - ar(r^2 + a^2)y \pm r(a^2 + r^2) \left(\frac{1}{r^3} - y\right)^{1/2}}{r \sqrt{1 - \frac{3}{r} - a^2 y \pm 2a \left(\frac{1}{r^3} - y\right)^{1/2}}}, \quad (10)$$

where \pm denotes the co-rotating orbit ($aL > 0$) and counter-rotating orbits ($aL < 0$), respectively.

For $0 < y \ll 1$, the stability of circular orbits is straightforward to analyze. The stability requirement $V''(r) \geq 0$ determines the range of the radii of the stable circular orbits, which is equivalent to

$$\frac{8ar^2 \sqrt{\frac{1}{r^3} - y} (r^3 y - 1) \pm r (6 - r - 15r^3 y + 4r^4 y) \pm a^2 (3 + r^2 y - 4r^5 y^2)}{2ar \sqrt{\frac{1}{r^3} - y} \pm (r - 3 - a^2 r y)} \leq 0. \quad (11)$$

Outside the horizon, this condition can be reduced to

$$r_{\text{ISCO}} < r < r_{\text{OSCO}}, \quad (12)$$

which defines the radii of the innermost stable circular orbit (ISCO) and the outermost stable circular orbit (OSCO). It is difficult to obtain the analytic form of r_{ISCO} and r_{OSCO} since Eq. (11) is related to high-order polynomials of r .

In the limit of $y \rightarrow 0$, Eq. (11) reduces to the condition of stable circular orbits in the Kerr spacetime. In such case, the OSCO does not exist, in other words, $\lim_{y \rightarrow 0} r_{\text{OSCO}} = \infty$. For a succinct analytical solution for r_{ISCO} in the Kerr spacetime, see [71]. When $y \neq 0$, the range of stable orbits will shrink as y increases for a fixed value of a , which is reflected in an increase of r_{ISCO} and a decrease of r_{OSCO} . And eventually, r_{ISCO} and r_{OSCO} will be equal and then cross at a specific value of y , at which point the stable orbits disappear. However, when y is fixed, the stability range for co-rotating orbits will expand as a increases, while that for counter-rotating will shrink. At a specific value of a , the stability range can be also vanished. In Figure 1, it shows how the allowable region of the stable equatorial circular orbits varies with a and y . In the following, we will assume that $y \ll 1$ ¹, such that the ISCO and OSCO are separated far enough to allow for a stable equatorial accretion disk outside the black hole.

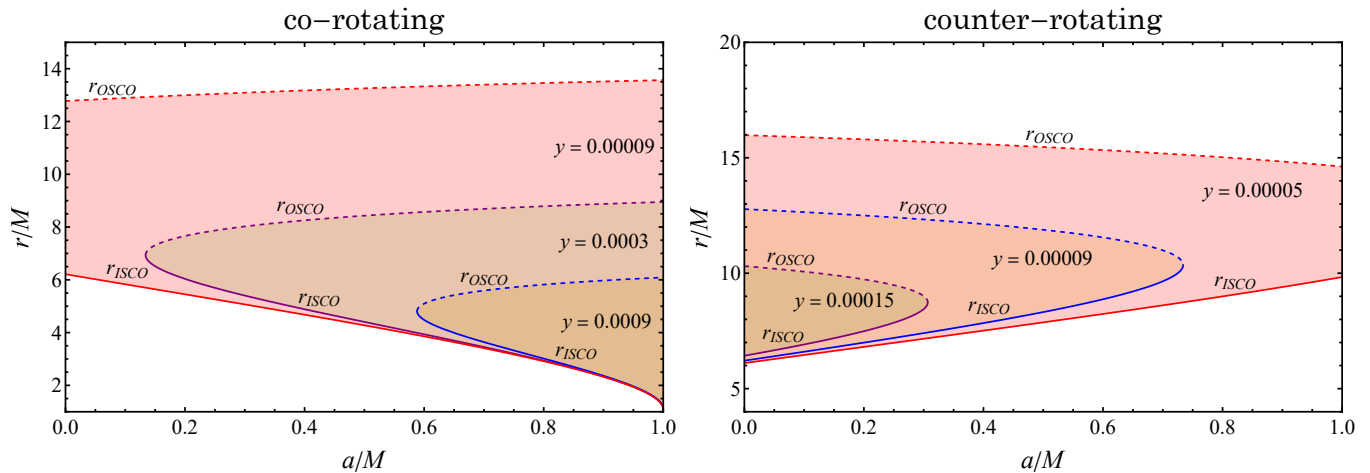


FIG. 1. The allowable region of the stable equatorial circular orbits in parameter $r \wedge a$ space. The solid curves and dashed curves represent $r_{\text{ISCO}}(a)$ and $r_{\text{OSCO}}(a)$ at different values of y , respectively. (Left) In the case of co-rotating orbits, from the outside to the inside, the solid or dashed curves with color (red, purple, blue) correspond to the values of y at (0.00009, 0.0003, 0.0009). (Right) In the case of counter-rotating orbits, from the outside to the inside, the solid or dashed curves with color (red, blue, purple) correspond to the values of y at (0.00005, 0.00009, 0.00015).

C. The thin disk model

The phenomenological model for M87* established in Kerr spacetime is proposed in [69], in which the accretion disk on the equatorial plane is assumed to be stationary, axisymmetric, and geometrically thin, and each particle in the disk moves along timelike geodesics. similar models were first used for Schwarzschild black holes with stationary emitters [42]. In this part, we introduce the thin accretion disk model applicable to Kerr-de Sitter spacetimes.

In this model, the accretion disk is divided into two parts: the part with stable circular orbits and the part with infalling orbits. For the former, $r_{\text{ISCO}} < r < r_{\text{OSCO}}$, a particle in the disk has constants of motion E_{\pm} and L_{\pm} as Eq. (9) and Eq. (10). Using Eq. (4), we obtain the particle's four-velocity as

$$\mathbf{u} = u^t \left(\partial_t + \frac{\pm \sqrt{\frac{1}{r^3} - y}}{\left(1 \pm a \sqrt{\frac{1}{r^3} - y}\right)} \partial_\phi \right), \quad u^t = \frac{\Xi \left(1 \pm a \sqrt{\frac{1}{r^3} - y}\right)}{\sqrt{1 - \frac{3}{r} \pm 2a \sqrt{\frac{1}{r^3} - y} - a^2 y}}, \quad (13)$$

¹ In Kerr-de Sitter spacetimes, the cosmological horizon r_C is governed by the cosmological constant as $r_C \approx \sqrt{1/y} - 1$. Since the observer is within the cosmological horizon, the cosmological horizon must be greater than the observation distance to conform to current assumptions about the size of the universe, which requires the cosmological constant to be much less than 1.

where \pm correspond to the co-rotating orbits and the counter-rotating orbits, respectively. For the latter, $r < r_{\text{ISCO}}$, we assume that the particle flows along the equatorial geodesic towards the event horizon with the same conserved quantities as that of ISCO:

$$u_\mu = (-E_{\text{ISCO}}, u_r, 0, L_{\text{ISCO}}). \quad (14)$$

Together with the condition $g^{\mu\nu}u_\mu u_\nu = -1$, we have

$$u_r = -\sqrt{-\frac{E_{\text{ISCO}}^2 g^{tt} - 2E_{\text{ISCO}} L_{\text{ISCO}} g^{t\phi} + L_{\text{ISCO}}^2 g^{\phi\phi} + 1}{g^{rr}}}. \quad (15)$$

Note that the accretion disk is not specified to be prograde or retrograde here, although the black holes with prograde accretion disk are the most frequently discussed in studies of black hole image. As shown in [section II B](#), the spacetime allows the existence of stable counter-rotating circular orbits, hence it cannot be ruled out that some astrophysical activity in the cosmos would create black holes with a stable retrograde accretion disk. In [section V](#), we will simulate the images of black holes with prograde and retrograde accretion disks, respectively.

III. LENSED IMAGES WITH THIN DISK MODEL

In this section, we present a comprehensive analytical approach for generating images of Kerr-de Sitter black holes. Firstly, the observer's screen is defined. Subsequently, a connection is established between each point on the observer's screen and the null geodesic parameterized by two conserved quantities (λ, η) . Finally, an equation is given to calculate the intensity of each point on the screen.

A. The observer's screen

Firstly, we define the specific spacetime region within which our analysis is conducted. In the case of reasonable parameter values (Λ, a, M) , the condition $\Delta_r = 0$ indicates the existence of four coordinate singularities known as horizons, namely r_{C-} , r_- , r_+ , and r_C (the cosmological horizon). These singularities act as dividing points, partitioning the spacetime into distinct regions [\[72\]](#). The region of primary interest to us is the interval $[r_+, r_C]$, commonly referred to as the domain of outer communication. In this context, we examine the scenario of an observer free-falling into a black hole while possessing zero angular momentum, also known as Zero Angular Momentum Observer (ZAMO). To describe the observer's local frame, we select an orthonormal tetrad denoted as $\{\mathbf{e}_{\hat{\mu}}\}$ [\[61\]](#):

$$\begin{aligned} \mathbf{e}_{\hat{t}} &= \zeta \partial_t + \gamma \partial_\phi, & \mathbf{e}_{\hat{r}} &= \frac{1}{\sqrt{g_{rr}}} \partial_r, \\ \mathbf{e}_{\hat{\theta}} &= \frac{1}{\sqrt{g_{\theta\theta}}} \partial_\theta, & \mathbf{e}_{\hat{\phi}} &= \frac{1}{\sqrt{g_{\phi\phi}}} \partial_\phi, \\ \gamma &= -\frac{g_{t\phi}}{g_{\phi\phi}} \sqrt{\frac{g_{\phi\phi}}{g_{t\phi}^2 - g_{tt}g_{\phi\phi}}}, & \zeta &= \sqrt{\frac{g_{\phi\phi}}{g_{t\phi}^2 - g_{tt}g_{\phi\phi}}}. \end{aligned} \quad (16)$$

Assuming that any photon reaching the observer's position will be measured by the observer, the general form of the 4-momentum of a photon is given by [Eq. \(4\)](#) with $\mu = 0$. In this context, we use k_μ to represent the momentum of the photon. Therefore, the 4-momentum of a photon measured by a ZAMO can be expressed as $P^{\hat{\mu}} = \eta^{\hat{\mu}\nu} e_{\hat{\nu}}^\xi k_\xi$, where each component is calculated as follows:

$$\begin{aligned} P^{\hat{t}} &= E(\zeta - \gamma\lambda), & P^{\hat{r}} &= E \frac{1}{\sqrt{g_{rr}}} \frac{\pm_r \sqrt{R(r)}}{\Delta_r}, \\ P^{\hat{\theta}} &= E \frac{1}{\sqrt{g_{\theta\theta}}} \frac{\pm_\theta \sqrt{\Theta(\theta)}}{\Delta_\theta}, & P^{\hat{\phi}} &= E \frac{\lambda}{\sqrt{g_{\phi\phi}}}. \end{aligned} \quad (17)$$

The relation between the celestial coordinates (ϑ, Φ) and the local measurement of photons' four-momentum is as follows:

$$P^{\hat{\phi}} = |P| \sin \Phi \cos \vartheta, P^{\hat{\theta}} = |P| \sin \vartheta, P^{\hat{r}} = |P| \cos \Phi \cos \vartheta, P^{\hat{t}} = |P|. \quad (18)$$

To display the image on a two-dimensional screen, we project the celestial coordinates onto a plane that faces the black hole [61]. The ‘screen coordinates’ (α, β) are related to the celestial coordinates as follows:

$$\alpha = -r_0 \tan \Phi, \quad \beta = r_0 \frac{\tan \vartheta}{\cos \Phi}. \quad (19)$$

When a photon with four-momentum k_μ reaches the observer’s position $(t_0, r_0, \theta_0, \phi_0)$, it is displayed on the observer’s screen. By combining the equations Eq. (19), Eq. (18), and Eq. (17), we obtain the following relationship:

$$\begin{aligned} \beta(\lambda, \eta) &= r \frac{P^{\hat{\theta}}}{P^{\hat{r}}} = \pm_{\theta} r \frac{\sqrt{g_{rr}} \Delta_r \sqrt{\Theta(\theta; \lambda, \eta)}}{\sqrt{g_{\theta\theta}} \Delta_\theta \sqrt{R(r; \lambda, \eta)}} \Bigg|_{(r_0, \theta_0)}, \\ \alpha(\lambda, \eta) &= -r \frac{P^{\hat{\phi}}}{P^{\hat{r}}} = r \frac{\sqrt{g_{rr}} \Delta_r \lambda}{\sqrt{g_{\phi\phi}} \sqrt{R(r; \lambda, \eta)}} \Bigg|_{(r_0, \theta_0)}. \end{aligned} \quad (20)$$

In fact, Eq. (20) establishes a connection between each point on the observer’s screen and a null geodesic parameterized by two conserved quantities (λ, η) . Since spacetime is stationary and axisymmetric, the coordinates t_0 and ϕ_0 are unconstrained. Eq. (20) is a key formula used in constructing the image of black holes. It can be solved inversely for any point (α, β) on the screen to obtain the two conserved quantities (λ, η) associated with the corresponding null rays. By integrating the geodesic equation, the path of the light ray can be traced backward to infinity or the outer horizon. Fortunately, Eq. (20) is completely invertible, the analytic formulas for $\lambda(\alpha, \beta)$ and $\eta(\alpha, \beta)$ are provided in Equations Eq. (A7) and Eq. (A8), respectively.

B. Observed luminosity

To calculate the observed intensity at each point (α, β) on the screen, we need to trace the corresponding light ray backward to infinity or the outer horizon and record each emitting region it passes through. We then add up the emission intensity from all the regions that intersect with the ray. In our case, the only emission region is the accretion disk on the equatorial plane, which is geometrically thin and axisymmetric. Therefore, it is sufficient to record the radius at which the ray intersects the equatorial plane.

After considering the gravitational redshift and neglecting the interaction between the light and the accretion disk, the observed luminosity at a point (α, β) on the image plane can be expressed as: [44]

$$I(\alpha, \beta) = \sum_{m=1}^{m_{\max}} f_m j_{\text{model}}(r_m) g^3(r_m, \alpha, \beta), \quad (21)$$

where r_m represents the radius at which the ray intersects the equatorial plane for the m^{th} time, m_{\max} is the maximum number of equatorial crossings. $j_{\text{model}}(r_m)$ denotes the emissivity per unit volume at a specific frequency, and $g(r_m, \alpha, \beta)$ represents the redshift factor, which is the observed frequency divided by the emission frequency, at radius r_m . The factor g^3 applies to the intensity of a specific frequency (for instance, 230 GHz image), while g^4 is suitable for integrated intensity $\int I d\nu$ [64]. f_m is an optional parameter known as the ‘fudge factor’ that controls the brightness of the higher-order photon ring.

In [44], the authors adopt $f_1 = 1$ and $f_{m>1} = 2/3$ to best match the time-averaged images for the radiative GRMHD simulation. We follow the same setting for f_m even though its effect on the overall image is minimal.

In section II C, we divided the accretion disk into two parts with different orbits. Consequently, the redshift factor is expressed as follows:

$$g = \frac{\nu_{\text{obs}}}{\nu_{\text{em}}} = \frac{k_\mu u_{\text{obs}}^\mu}{k_\mu u_{\text{em}}^\mu} = \begin{cases} g_{\text{circular}}(r, \lambda, \eta) & r_{\text{ISCO}} < r < r_{\text{OSCO}} \\ g_{\text{infall}}(r, \lambda, \eta, \nu_r) & r_H < r < r_{\text{ISCO}} \end{cases}, \quad (22)$$

and the analytical formulas for g_{circular} and g_{infall} are provided in Eq. (B1) and Eq. (B4).

Based on previous studies investigating black hole accretion disks [73, 74], the emissivity $j(r)$ exhibits a significant decrease as the radius r increases. In line with the model employed to fit the 1.3 mm (230 GHz) wavelength image of M87* in Chael et al.’s work [44], we choose the emissivity as

$$\text{Log}[j_{\text{model}}(r)] = -2\text{Log}[r/r_+] - \frac{1}{2}\text{Log}[r/r_+]^2, \quad (23)$$

which has also been utilized for simulating images of Kerr-Melvin black holes [75].

To explicitly simulate the image of Kerr-de Sitter black holes using Eq. (21), we still need the specific expressions for r_m and m_{\max} , which are uniquely determined by the screen coordinates (α, β) through complex analytic ray tracing. In the next section, we present a complete derivation of r_m and m_{\max} . By separately addressing the equations for r and θ , we obtain Eq. (42) and Eq. (43) as the respective forms of r_m and m_{\max} .

IV. ANALYTIC RAY TRACING

Refs. [37] and [76] have provided complete analytic solutions for null geodesics and derived the analytical formulas for $r_m(\alpha, \beta)$ and $m_{\max}(\alpha, \beta)$ in Kerr spacetimes. Additionally, in [77] the authors obtained analytic solutions in terms of elliptic integrals for near-bound null geodesics in Kerr-de Sitter spacetimes. Building upon these previous works, we derive expressions of $r_m(\alpha, \beta)$ and $m_{\max}(\alpha, \beta)$ that apply to Kerr-de Sitter spacetimes.

The null geodesic equations for r and θ are derived from Eq. (6) as follows:

$$\frac{\Sigma}{E} p^r = \pm_r \sqrt{R(r)}, \quad \frac{\Sigma}{E} p^\theta = \pm_\theta \sqrt{\Theta(\theta)}, \quad (24)$$

where $R(r)$ and $\Theta(\theta)$ are given in Eq. (7). The common approach to decoupling geodesic equations is to parameterize the geodesics using the ‘Mino time’ τ [78], defined as:

$$\frac{dx^\mu}{d\tau} = \frac{\Sigma}{E} p^\mu. \quad (25)$$

Using this parameterization, the total Mino time that a photon experiences from the observer’s position (r_0, θ_0) to the emitting source’s position (r_s, θ_s) can be expressed as:

$$\int_{r_0}^{r_s} \frac{dr}{\pm_r \sqrt{R(r)}} = I_r, \quad (26a)$$

$$\int_{\theta_0}^{\theta_s} \frac{d\theta}{\pm_\theta \sqrt{\Theta(\theta)}} = G_\theta, \quad (26b)$$

$$I_r = G_\theta = \int d\tau, \quad (26c)$$

where the integrals represent integration along the path. The plus or minus signs, \pm_r and \pm_θ , are chosen depending on the direction of integration.

A. Radial equation

We now turn our attention to the radial equation. Introducing the radial roots (r_1, r_2, r_3, r_4) , which satisfy the following relation:

$$R(r) = \mathcal{E}^2 (r - r_1)(r - r_2)(r - r_3)(r - r_4) = 0, \quad (27)$$

with

$$\mathcal{E} = \sqrt{\frac{\eta\Lambda}{3} + \Xi^2 + \frac{1}{3}a^2\Lambda\Xi^2 - \frac{2}{3}a\lambda\Lambda\Xi^2 + \frac{1}{3}\lambda^2\Lambda\Xi^2}. \quad (28)$$

These radial roots are determined by the parameters (λ, η) of the null geodesics, and their analytical solutions can be obtained by Ferrari’s method [77]. We are particularly interested in the geodesics near the black hole, which can be classified into two groups based on their associated radial roots:

1. Geodesics with four real roots $(r_1 < r_2 < r_3 < r_4)$, where $r_0 > r_4 > r_+$. These geodesics have one turning point and extend to infinity.
2. Geodesics that never encounter a turning point and eventually cross the event horizon.

Therefore, the total Mino time I_r^{total} required for light rays from the observer to reach either infinity or the horizon can be expressed as:

$$I_r^{\text{total}} = \begin{cases} -\int_{r_0}^{r_4} \frac{dr}{\sqrt{R(r)}} + \int_{r_4}^{\infty} \frac{dr}{\sqrt{R(r)}} & r_0 > r_4 > r_+, \\ -\int_{r_0}^{r_+} \frac{dr}{\sqrt{R(r)}} & r_4 \in \mathbb{C} \text{ or } r_4 < r_+. \end{cases} \quad (29)$$

To obtain the expression for $r(\tau)$, the radial equation need to be solved for different cases.²

For the cases where $r_4 \in \mathbb{R}$, solving Eq. (26a) in reverse provides the solution:

$$r(I_r) = \frac{r_3 r_{14} \text{sn}^2(g_E I_r + \nu_r F(\phi_{E,0}|k_E)|k_E) + r_4 r_{31}}{r_{14} \text{sn}^2(g_E I_r + \nu_r F(\phi_{E,0}|k_E)|k_E) + r_{31}} \quad (r_4 \in \mathbb{R}), \quad (30)$$

where $\text{sn}(\phi|k)$ is the Jacobi elliptic sine function [79], $F(\phi|k)$ is the elliptic integral of the first kind, and

$$\begin{aligned} r_{ij} &= r_i - r_j, & k_E &= \frac{r_{41} r_{32}}{r_{42} r_{31}}, \\ g_E &= \frac{\mathcal{E} \sqrt{r_{42} r_{31}}}{2}, & \phi_{E,i} &= \arcsin\left(\sqrt{\frac{r_{31} r_{i4}}{r_{41} r_{i3}}}\right). \end{aligned} \quad (31)$$

For the cases where $r_4 = \bar{r}_3 \in \mathbb{C}$, the inverse solution of Eq. (26a) yields

$$r(I_r) = \frac{(r_2 B + A r_1) \text{cn}\left(\mathcal{E} \sqrt{AB} I_r + \nu_r F(\phi_{P,0}|k_P)|k_P\right) + (r_2 B - A r_1)}{(B + A) \text{cn}\left(\mathcal{E} \sqrt{AB} I_r + \nu_r F(\phi_{P,0}|k_P)|k_P\right) + (B - A)} \quad (r_4 = \bar{r}_3 \in \mathbb{C}), \quad (32)$$

where $\text{cn}(\phi|k)$ is the Jacobi elliptic cosine function [79], and

$$\begin{aligned} A &= \sqrt{r_{32} r_{42}}, & B &= \sqrt{r_{31} r_{41}}, \\ k_P &= \frac{(B + A)^2 - (r_2 - r_1)^2}{4AB}, & \phi_{P,i} &= \arccos\left(\frac{(A - B)r_i + r_2 B - r_1 A}{(A + B)r_i - r_2 B - r_1 A}\right). \end{aligned} \quad (33)$$

The independent variable I_r in Eq. (30) or Eq. (32) is limited to the range $0 < I_r < I_r^{\text{total}}$, where

$$I_r^{\text{total}} = \begin{cases} -g_E [F(\phi_{E,4}|k_E) - F(\phi_{E,0}|k_E)] + g_E [F(\phi_{E,\infty}|k_E) - F(\phi_{E,4}|k_E)] & r_4 > r_+ \in \mathbb{R}, \\ -g_E [F(\phi_{E,+}|k_E) - F(\phi_{E,0}|k_E)] & r_4 < r_+ \in \mathbb{R}, \\ -\frac{1}{\mathcal{E} \sqrt{AB}} [F(\phi_{P,+}|k_P) - F(\phi_{P,0}|k_P)] & r_4 = \bar{r}_3 \in \mathbb{C}. \end{cases} \quad (34)$$

Eq. (30) and Eq. (32) together constitute the solution of the radial equation in the domain of outer communication, which will be used to calculate the radius r_m of the photon when it crosses the equatorial plane for the m^{th} time.

B. Angular integrals

In this part, we obtain the Mino time experienced by photons when they cross the equatorial plane by addressing the angular integral.

Letting $u = \cos^2 \theta$, the angular potential $\Theta(\theta)$ can be written as

$$\Theta(\theta) = \frac{1}{1-u} \mathcal{U}(u - u_+) (u - u_-), \quad (35)$$

$$\mathcal{U} = -\frac{1}{3} a^2 \eta \Lambda - a^2 \Xi^2 - \frac{1}{3} a^4 \Lambda \Xi^2 + \frac{2}{3} a^3 \lambda \Lambda \Xi^2 - \frac{1}{3} a^2 \lambda^2 \Lambda \Xi^2, \quad (36)$$

with

$$\begin{aligned} u_{\pm} &= \Delta \pm \sqrt{\frac{3\eta}{a^2 (\Lambda (\Xi^2 (a - \lambda)^2 + \eta) + 3\Xi^2)} + \Delta^2}, \\ \Delta &= \frac{\eta (a^2 \Lambda - 3) + \Xi^2 (a - \lambda) (a^3 \Lambda - a^2 \lambda \Lambda + 3a + 3\lambda)}{2a^2 (\Lambda (\Xi^2 (a - \lambda)^2 + \eta) + 3\Xi^2)}. \end{aligned} \quad (37)$$

² For detailed calculations, please refer to [76] or [77].

As demonstrated in [77], a photon following ordinary geodesics ($\eta > 0$) undergoes libration between $\theta_+ = \arccos(\sqrt{u_+})$ and $\theta_- = \arccos(-\sqrt{u_+})$, crossing the equatorial plane each time. Consequently, the path integral in Eq. (26b) can be expanded and expressed as:

$$G_\theta(\theta_s) = 2m \left| \int_{\pi/2}^{\theta_\pm} \frac{d\theta}{\sqrt{\Theta(\theta)}} \right| + \eta_0 \left| \int_{\pi/2}^{\theta_0} \frac{d\theta}{\sqrt{\Theta(\theta)}} \right| - \eta_s \left| \int_{\pi/2}^{\theta_s} \frac{d\theta}{\sqrt{\Theta(\theta)}} \right|, \quad (38)$$

where m represents the number of times the ray reaches the equatorial plane, and

$$\eta_i = \text{sign}(p_\theta \cos \theta)|_{\theta=\theta_i}. \quad (39)$$

After reducing the integral to the form of elliptic integrals, we can obtain the Mino time it takes for the ray to reach the equatorial plane for the m^{th} time as follows:

$$G_m = \frac{2(m - H(\eta_0))}{\sqrt{-u_- \bar{U}}} K\left(\frac{u_+}{u_-}\right) + \frac{\eta_0}{\sqrt{-u_- \bar{U}}} F\left(x_0 \left| \frac{u_+}{u_-} \right.\right), \quad (40)$$

where H denotes the Heaviside function [79], and

$$x_0 = \arcsin \sqrt{\frac{\cos^2 \theta_0}{u_+}}. \quad (41)$$

By utilizing Eq. (30) or Eq. (32), we can determine the radius $r_m(\alpha, \beta)$ at which the ray crosses the equatorial plane for the m^{th} time as follows:

$$r_m(\alpha, \beta) = r(G_m), \quad (42)$$

while $0 < G_m < I_r^{\text{total}}$, and the maximal value of m is

$$m_{\text{max}} = \left\lfloor \frac{\sqrt{-u_- \bar{U}} I_r^{\text{total}} - \eta_\theta F\left(x_0 \left| \frac{u_+}{u_-} \right.\right)}{2K\left(\frac{u_+}{u_-}\right)} - H(\eta_0) \right\rfloor, \quad (43)$$

where I_r^{total} is given in Eq. (34), and the bracket indicates the rounding down operation.

V. SIMULATIONS

The mathematical preparations for simulating images of Kerr-de Sitter black holes have now been completed. In this section, we explore the potential effects of the cosmological constant on black hole observations through various simulations. These simulations encompass the overall visual appearance of the black hole images, the characteristics of the observed curves, the relative size of the images, and the observed intensity. By conducting these simulations, we aim to gain insights into the impact of the cosmological constant on the observations of black holes.

A. Images with prograde and retrograde disk

We use Eq. (21) to generate simulated images of Kerr-de Sitter black holes. Recall that our model is a generalization of the M87* analytic model developed by [44]. While [44] considered a static observer at infinity and utilized broken power-law fitting functions to represent the 4-velocity of accreting gas, we consider a ZAMO and describe the 4-velocity of the accreting gas using precise time-like orbits in Kerr-de Sitter spacetimes. Additionally, our choices of the emissivity in Eq. (23) and the ‘fudge’ factor in Eq. (21) align with those of [44].

In Figure 2 and Figure 3, we present simulations of the observations of Kerr-de Sitter black holes with prograde Figure 2 and retrograde Figure 3 accretion disks, respectively. We set the dimensionless cosmological constant to $y = 0.00003$ for both cases. For different values of the black hole spin $a = (0.1, 0.66, 0.9, 0.999)M$, we examine the observation inclination angles $\theta_0 = (1^\circ, 45^\circ, 75^\circ, 88^\circ)$, respectively. The observation distance remains fixed at $r_0 = 50M$, and the observer’s screen range is restricted to $-10 < \alpha/M < 10$ and $-10 < \beta/M < 10$.

As demonstrated in our simulated images, the presence of the OSCO in Kerr-de Sitter spacetimes leads to the clear visibility of the outer boundary of the accretion disk when the observer inclination is close to 90 degrees. Each image exhibits a distinct bright ring, known as the ‘photon ring’, which closely aligns with the critical curve. The dark regions at the center correspond to the event horizon of the black hole. Overall, the presence of a cosmological constant has minimal impact on the visual appearance of the black hole.

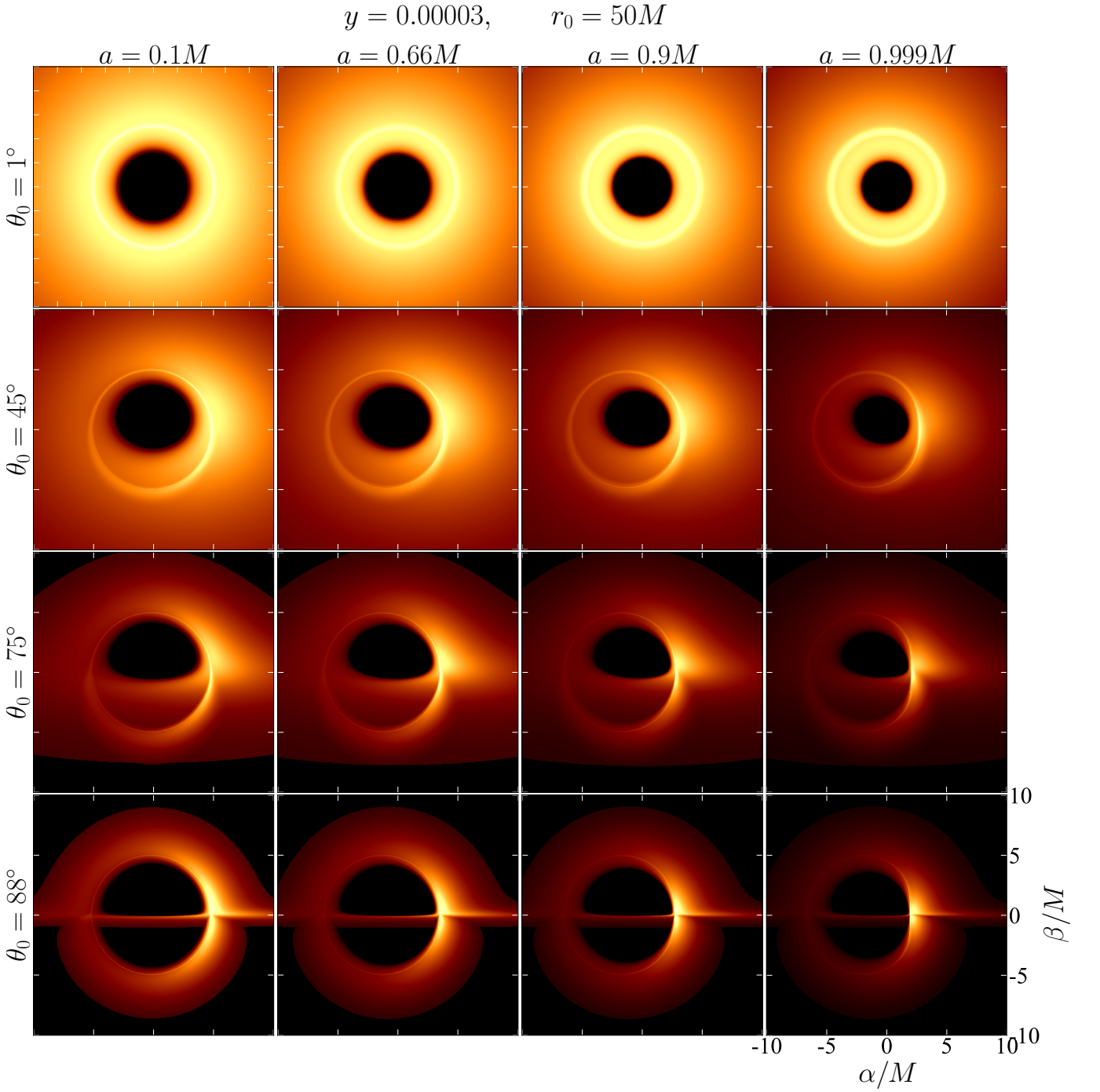


FIG. 2. The images depict Kerr-de Sitter black holes illuminated by a prograde thin equatorial accretion disk. In these simulations, the dimensionless cosmological constant is fixed at $y = 0.00003$, and the radial observation distance r_0 is consistently set at $50M$ from the black hole. The columns, from left to right, represent models with spins $a = (0.1, 0.66, 0.9, 0.999)$, while the rows, from top to bottom, display observations at inclinations $\theta_0 = (1^\circ, 45^\circ, 75^\circ, 88^\circ)$. For each graph, the intensity data is independently normalized and then mapped to colors using the colormap 'afmhot', employing a power function with an index of $\gamma = 1/4$.

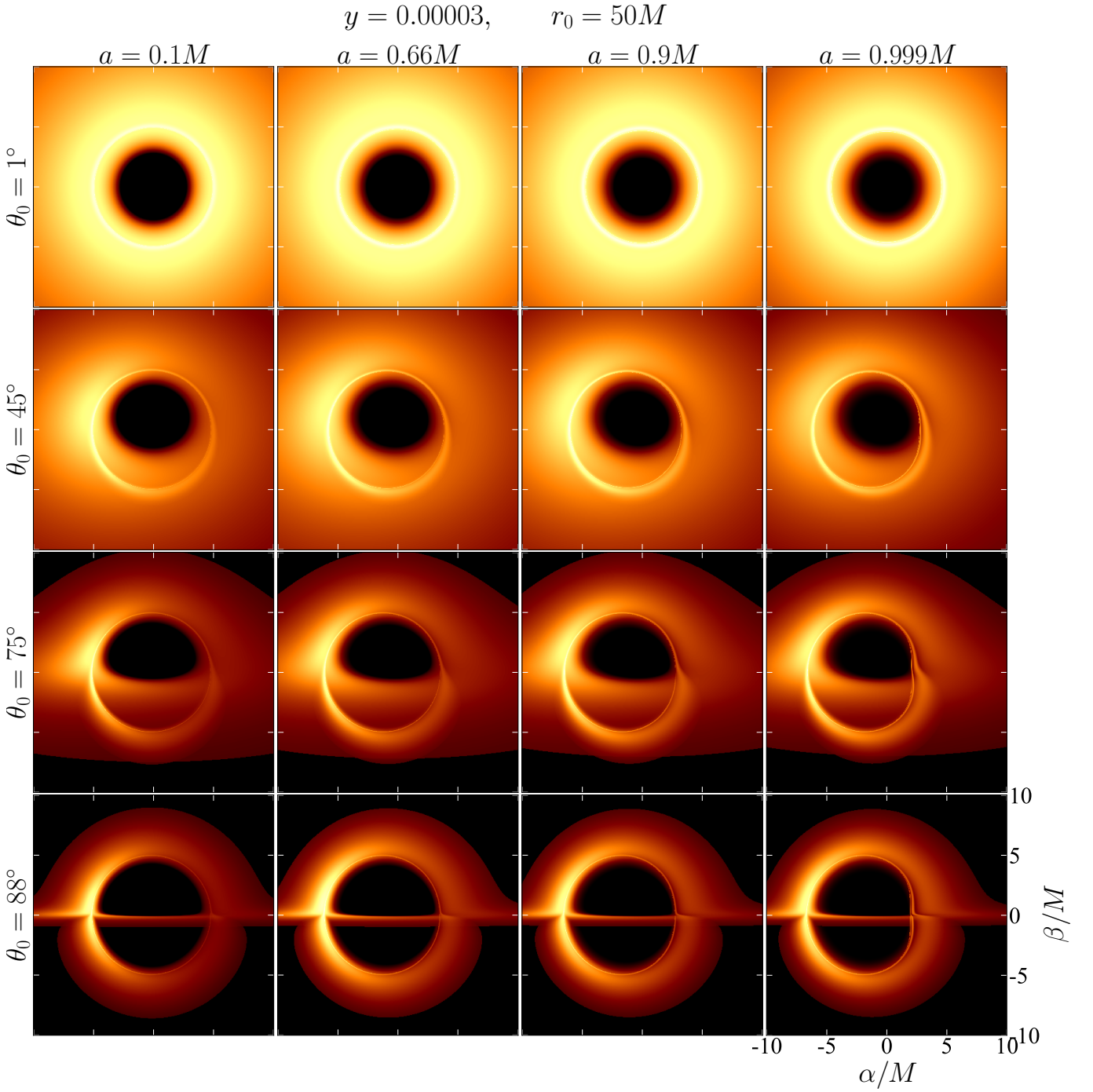


FIG. 3. The images portray Kerr-de Sitter black holes illuminated by a retrograde thin equatorial accretion disk. In these simulations, the dimensionless cosmological constant is fixed at $y = 0.00003$, and the radial observation distance r_0 remains consistently $50M$ away from the black hole. The columns, from left to right, represent models with spins $a = (0.1, 0.66, 0.9, 0.999)M$, while the rows, from top to bottom, display observations at inclinations $\theta_0 = (1^\circ, 45^\circ, 75^\circ, 88^\circ)$. For each graph, the intensity data is independently normalized and mapped to colors using the color map 'afmhot', employing a power function with an index of $\gamma = 1/4$.

B. The characteristic curves

To analyze the geometric details of black hole images, a straightforward approach is to plot the various geometric boundaries of the model directly on the observer's screen. These boundaries represent the apparent positions of the geometric features. A light source can have an infinite number of apparent positions because the emitted ray can travel around the black hole any number of times before reaching the observer. Each apparent position is labeled with a number $m = 1, 2, 3, \dots$, where even m corresponds to the back of the equatorial disk and odd m corresponds to the front of the disk.

For the entire equatorial emission surface, its image on the observer's screen appears as infinitely many rings, known as photon rings [37, 43]. Each photon ring represents a miniature image of the entire equatorial plane. Consequently, the m^{th} order image of a curve on the equatorial plane is confined to the m^{th} order photon ring. As m approaches infinity, the width of the photon rings becomes negligible, allowing us to describe the photon ring as a closed curve \mathcal{C} , commonly known as the photon's 'critical curve'.

The photon's critical curve \mathcal{C} has been extensively studied in previous works [40, 67, 68]. In terms of screen coordinates, using Eq. (20), the curve \mathcal{C} can be expressed as:

$$\vec{\mathcal{C}}(R) = (\alpha(\lambda(R), \eta(R)), \pm\beta(\lambda(R), \eta(R))) \quad R \in [r_+^\gamma, r_-^\gamma], \quad (44)$$

where $\lambda(R)$, $\eta(R)$ and r_\pm^γ are derived in section C. In addition to the critical curve, we are also interested in other characteristic curves defined by a constant Boyer-Lindquist radius $r = \text{const.}$, particularly the equatorial horizon and the ISCO. These curves, in screen coordinates, can be represented by the equation

$$r_m(\alpha, \beta) = \text{const.}, \quad (45)$$

where $r_m(\alpha, \beta)$ is defined in Eq. (42).

In Figure 4, we present several characteristic curves of different black hole models. These include the direct image ($m = 1$) of the equatorial horizon, the ISCO, and the circular orbit at $r = 2(r_H + r_{\text{ISCO}})$. We also show the lensed image ($m = 2$) of the equatorial horizon and the critical curve.

C. The relative size

Previous studies on the black hole shadow have revealed that the cosmological constant leads to a reduction in the size of the shadow [40, 67]. As depicted in Figure 4, the other characteristic curves of the black hole also diminish in size in proportion to the critical curve. Consequently, it is evident that the overall black hole image will shrink accordingly. To illustrate this phenomenon, we showcase Figure 5, featuring simulated images of black holes at varying cosmological constants.

While previous discussions concentrated on a fixed observation distance r_0 , the presence of a cosmological constant introduces a notable influence on the relative size of the black hole shadow and image, which is further contingent on the observation distance. To scrutinize the correlation between the relative size of the black hole, the cosmological constant, and the observation distance, we introduce a parameter ρ_w as a representation of the black hole's relative size.

For simplicity, we will adopt a fixed observation inclination ($\theta_0 = 90^\circ$) and black hole spin ($a = 0.9M$), exclusively directing our attention to the discussion of the black hole's relative size. In the context of this analysis, the parameter ρ_w is defined as the horizontal radius of the black hole shadow, as illustrated in Figure 6. Consequently, ρ_w is concisely expressed as:

$$\rho_w = \alpha(\lambda(r_+^\gamma), \eta(r_+^\gamma)) - \alpha(\lambda(r_-^\gamma), \eta(r_-^\gamma)), \quad (46)$$

where $\alpha(\lambda, \eta)$ is given in Eq. (20), $\lambda(R)$, $\eta(R)$ and r_\pm^γ are given in section C.

In Figure 7, the demonstration reveals that the relative size ρ_w of the black hole diminishes with increasing observation distance r_0 or cosmological constant. Noteworthy is the consistent reduction of the relative size to zero as the limit $r_0 \rightarrow r_C$ is approached, where r_C signifies the cosmological horizon introduced at the outset of section III A. This observation prompts an investigation into the correlation between the relative size and the relative observation position r_0/r_C .

As depicted in Figure 8, the relative size of the black hole remains largely constant when the relative observation position is fixed, showing minimal influence from the cosmological constant. Nevertheless, with a non-vanishing cosmological constant, the relative size of the black hole consistently decreases as the observer moves farther away from it.

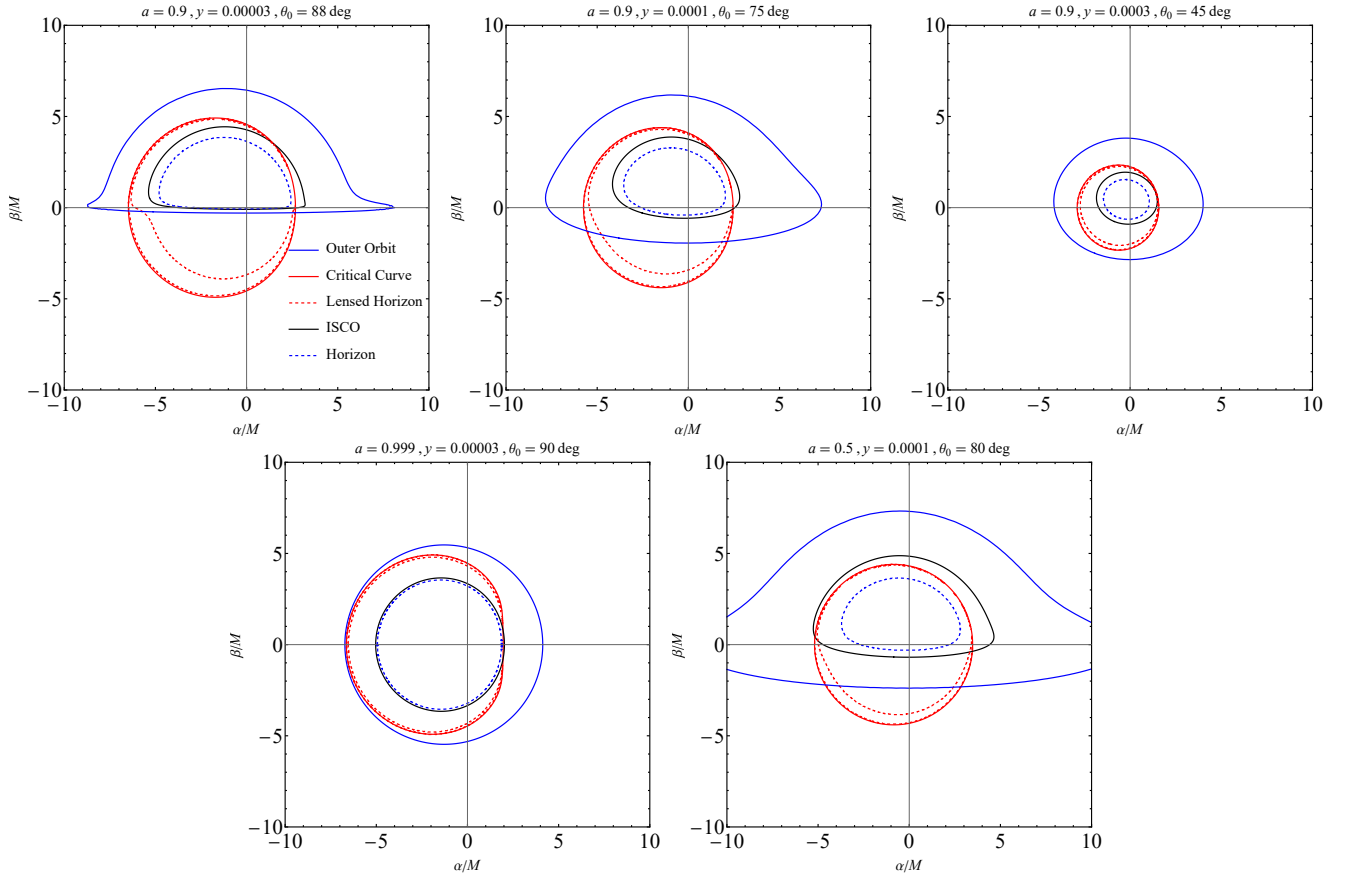


FIG. 4. The characteristic curves depicted in the figure depend on the black hole spin, cosmological constant, and observer inclination. The red solid curves represent the critical curve of photons. The blue solid lines correspond to the direct image ($m = 1$) of the equatorial circular orbit with a constant Boyer-Lindquist radius $r = 2(r_H + r_{\text{ISCO}})$. The black solid lines represent the direct image ($m = 1$) of the ISCO. The red dashed lines represent the lensed image ($m = 2$) of the equatorial horizon. The blue dashed lines depict the direct image ($m = 1$) of the equatorial horizon. The specific black hole parameters and observer inclination are indicated at the top of each panel.

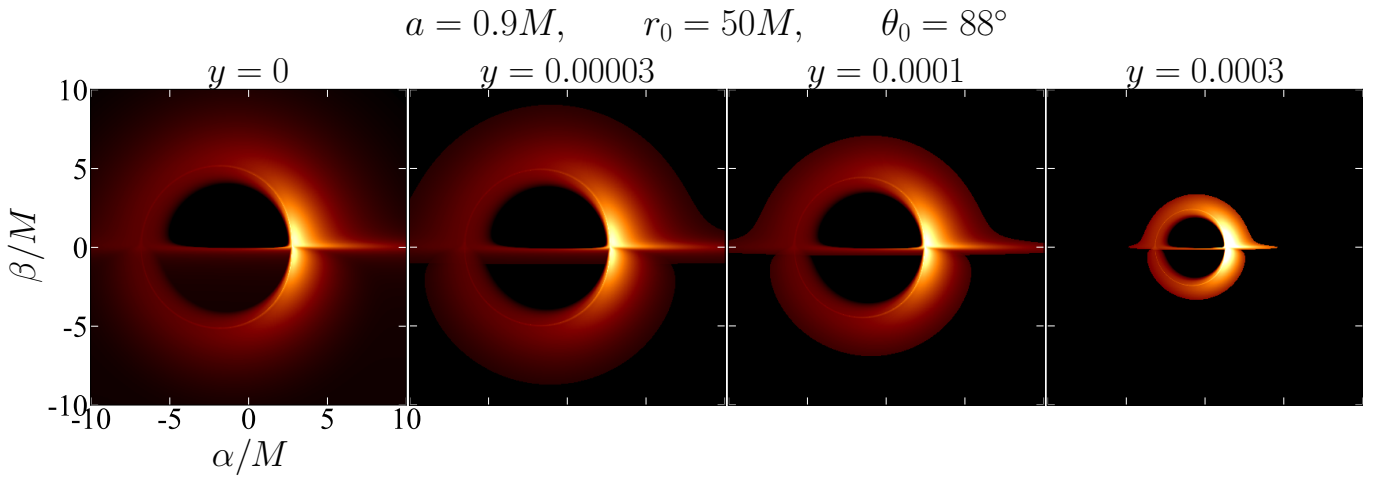


FIG. 5. Images of Kerr-de Sitter black holes with different cosmological constants. From left to right, the dimensionless cosmological constants are set as $y = (0, 0.00003, 0.0001, 0.0003)$. Each black hole in the figure has the same spin $a = 0.9$ and the observer's positions are fixed at $(r_0 = 50M, \theta_0 = 88^\circ)$.

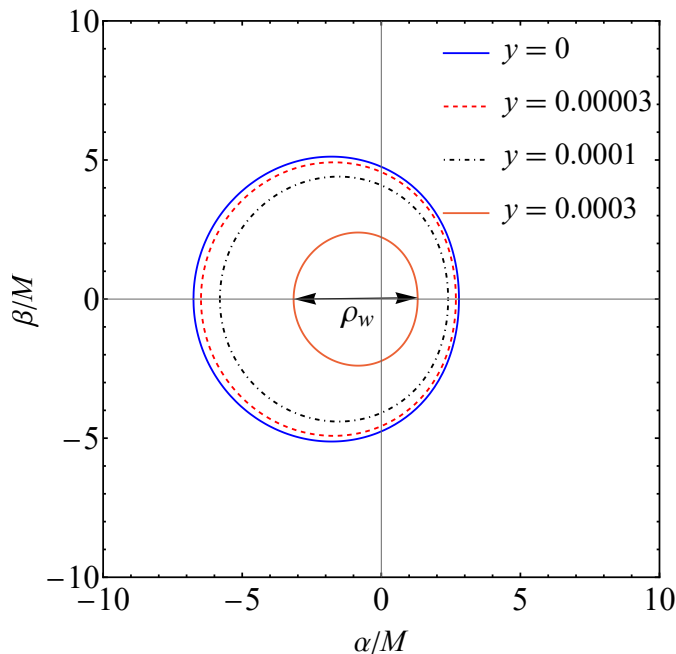


FIG. 6. The critical curves of the four black holes in Figure 5. The curves from outside to inside possess dimensionless cosmological constants $y = 0$ (blue solid), $y = 0.00003$ (red dashed), $y = 0.0001$ (blue dashed), and $y = 0.0003$ (red solid).

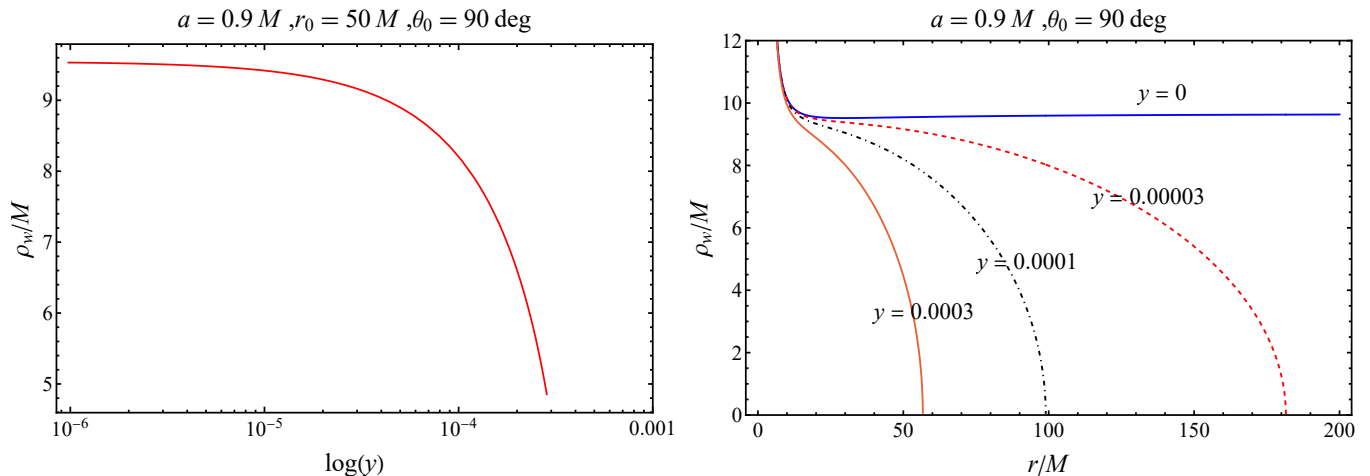


FIG. 7. The relative size of the shadow varies with respect to y (the dimensionless cosmological constant) or r (the observation distance).

D. Observed intensity

Another noteworthy observation from Figure 5 is the increased brightness of the black hole image as the cosmological constant rises. Recalling that Eq. (34) used to calculate the observed intensity does not take into account the cost of radiative transmission and the flux of light received by the observer. Thus, the observed intensity here can be understood as the luminosity of the accretion disk.

In Figure 9, we illustrate brightness cross-sections perpendicular and parallel to the projected spin axis, comparing cases with zero and non-zero cosmological constants. The black hole parameters and observer's position are $a = 0.9M$ and $(r_0 = 50M, \theta_0 = 75^\circ)$, respectively. It can be seen that the presence of the cosmological constant increases the peak value of the observation intensity, and the positions of the peaks on the left and right sides are closer together. This is consistent with the reduction and brightening of the photon ring shown by Figure 5.

To gain further insight into this luminance enhancement, we fix the cosmological constant and compare the observed

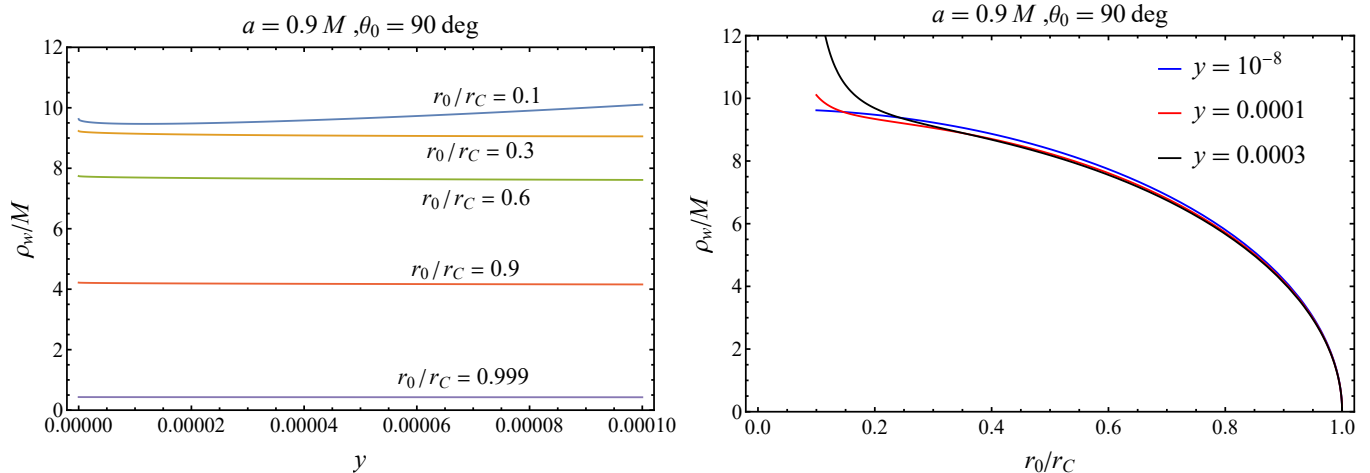


FIG. 8. The relative size of the shadow varies with respect to y (the dimensionless cosmological constant) or r/r_C (the relative observation distance)

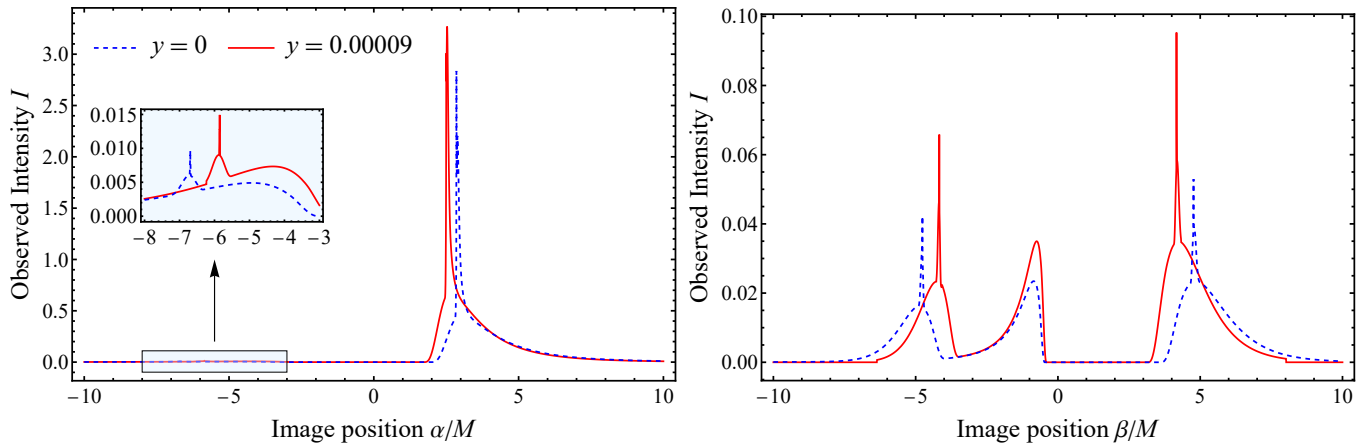


FIG. 9. Comparison of the observed intensity with and without a cosmological constant. The black hole spin is fixed at $a = 0.9$. The image on the left shows the observed intensity on the α -axis at β equals 0 by a ZAMO at position ($r_0 = 50M, \theta_0 = 75^\circ$), while the image on the right shows the observed intensity on the β -axis at α equals 0. The red solid lines are the case of $y = 0.00009$ and the blue dashed lines are that of Kerr cases.

intensity at different observation distances. Figure 10 illustrates that an observer at a distance of $r_0 = 100M$ will observe a smaller and brighter photon ring than an observer at $r_0 = 50M$. It should be noted that the increase in observed intensity shown in Figure 9 and Figure 10 is always accompanied by the position of the peaks on both sides being close to each other.

This property proposes a theoretically feasible method to test the cosmological constant, which is to image a black hole at different observation distances and analyze the change in the luminosity of the black hole with the change in the observer's position. With current black hole imaging technology, it is not practical to image black holes from beyond Earth. One possible solution is to take advantage of changes in observation distances caused by the relative motion of galaxies. Formulating a practical method is beyond the current scope of this paper.

VI. CONCLUSION

In this paper, we have developed a comprehensive analytic method for simulating images of Kerr-de Sitter black holes illuminated by equatorial thin accretion disks. The model of the equatorial accretion disk is established in section II C, assuming particles strictly follow equatorial geodesic motion. The range of stable circular orbits in the equatorial plane has been depicted in Figure 1.

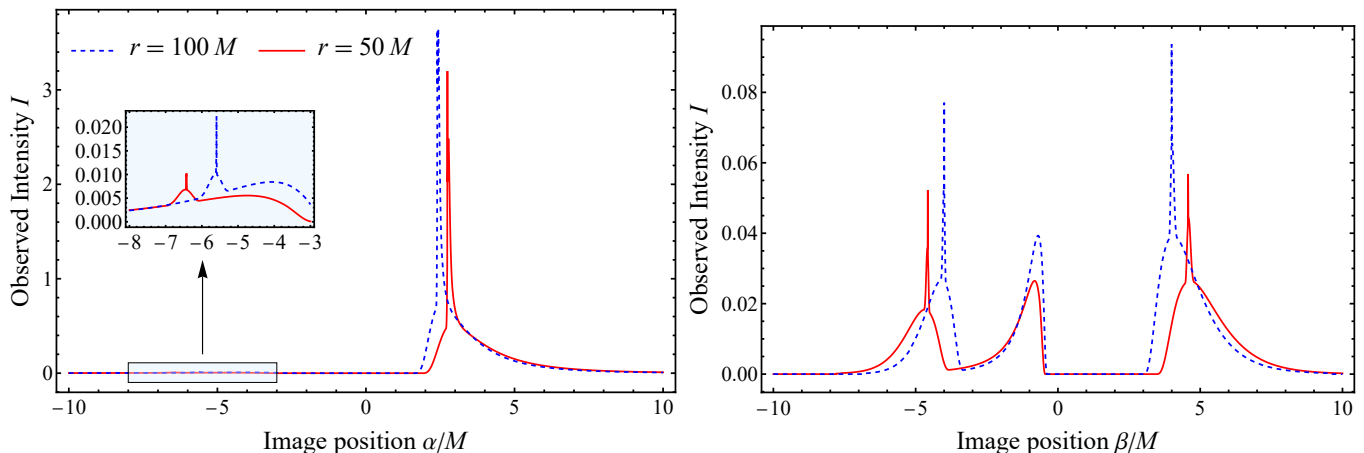


FIG. 10. Comparison of the observed intensity at different observation distances. The dimensionless cosmological constant is $y = 0.00003$, and the black hole spin is $a = 0.9$. The corresponding radius of the OSCO is approximately $180M$. The image on the left shows the intensity on the α -axis at $\beta = 0$ observed by a ZAMO at inclination ($\theta_0 = 75^\circ$), while the image on the right shows the observed intensity on the β -axis at $\alpha = 0$.

By considering a zero angular momentum observer within the domain of outer communication, we have traced the associated light rays backward through the emitting region to calculate the intensity at each screen position (α, β) . The formula Eq. (21) we use to generate the black hole image are fully explicit, as detailed in section III B and section IV.

Using these explicit expressions, we have simulated images of Kerr-de Sitter black holes illuminated by both prograde and retrograde accretion disks (Figure 2 and Figure 3). We have also investigated the effects of cosmological constants on characteristic curves (Figure 4), relative size (Figure 5, Figure 6 and Figure 8), and observed intensity (Figure 9 and Figure 10).

Before summarizing our results, we clarify the difference between the relative size and the apparent size of the black hole used in this paper. The apparent size is equivalent to the apparent diameter in astronomy, which is in line with our visual intuition that the farther away an object is, the smaller it looks. When our imaging focal length is a fixed value (for example, the focal length of the human eye is the distance from the lens to the retina), the size of the object in the image can be regarded as the apparent size. In most studies of black hole images, researchers usually set the distance between the observer and the black hole to be infinite. At this time, a fixed focal length will lead to an infinitesimal apparent size. To obtain a black hole image with a finite size, the common practice is to set the focal length as the distance from the observer to the black hole to eliminate the influence of infinite distance on the image size. In this paper, the definition of Eq. (19) is to set the focal length as the distance from the observer to the black hole, and consequently the size of the black hole image defined by Eq. (46) is called the relative size. The relative size is equivalent to the actual size of the object in flat spacetime. In curved spacetime it can be understood as the optically measurable size of an object. The distinction between relative size and apparent size is displayed in Figure 11.

Our results show that the effects of cosmological constants on black hole images are mainly reflected in two aspects: relative size and observed intensity. In flat spacetime, changes in observation distances do not affect the relative sizes of objects. In a Kerr spacetime, a distant observer will get similar results as in flat spacetime since the Kerr spacetime is asymptotically flat. However, in Kerr-de Sitter spacetimes with a cosmological constant $\Lambda > 0$, we find that the relative size of the black hole decreases with increasing observational distance and tends to zero as the observer approaches the cosmological horizon r_C (Figure 7). Furthermore, we find that the observer's position in the universe r_0/r_C determines the relative size of the black hole (Figure 8). Another notable effect of the cosmological constant on black hole images is the increase in luminosity, accompanied by a decrease in relative size (Figure 9 and Figure 10).

ACKNOWLEDGMENTS

This work is supported by National Science Foundation of China grant No. 11105091 and No. 12175099. We greatly appreciate the comments from Prof. Yongge Ma and Prof. Miao Li for very useful discussions.

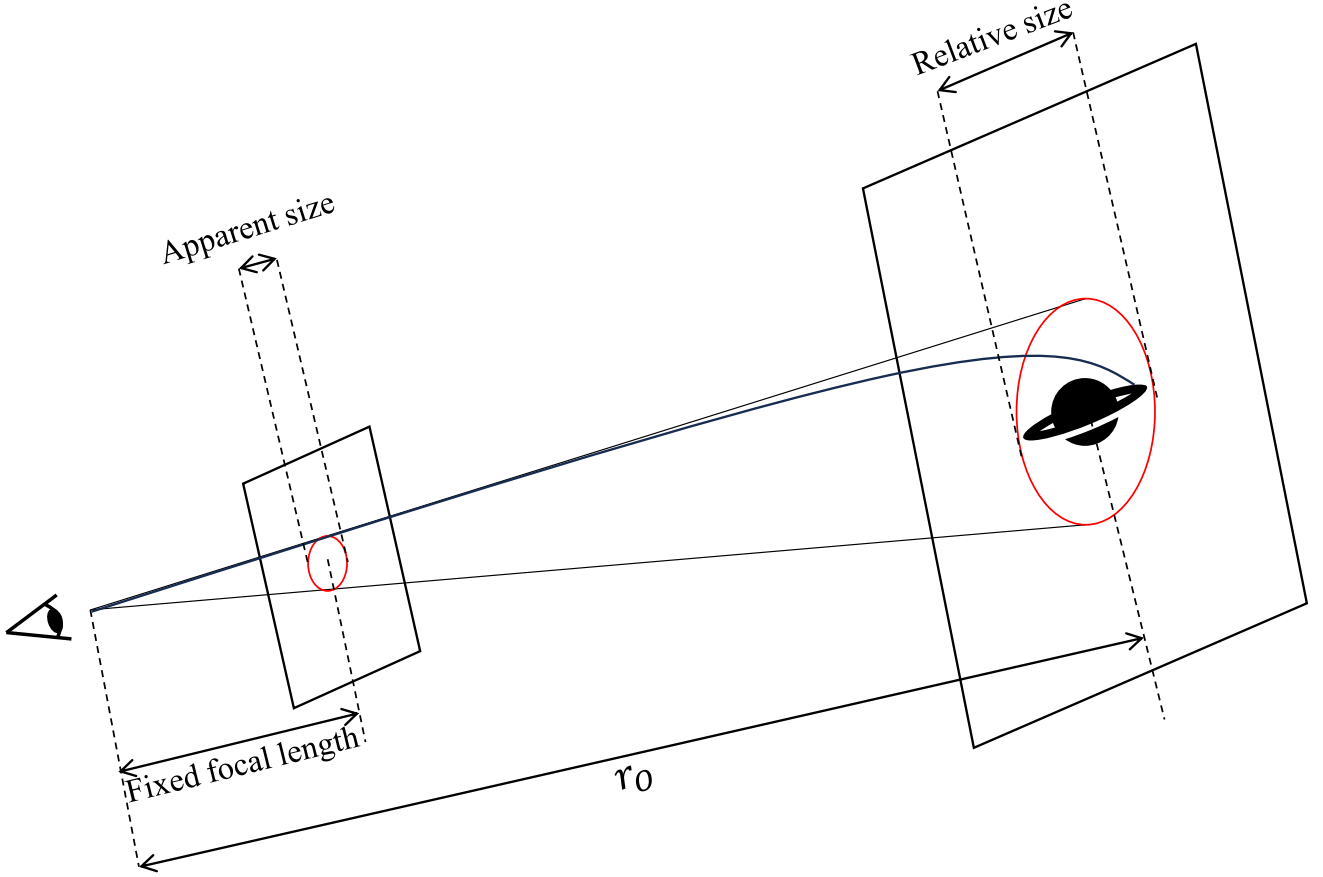


FIG. 11. A schematic diagram of the black hole imaging process. The apparent size of a black hole image corresponds to a fixed focal length. The relative size of a black hole image corresponds to a focal length equal to the distance from the observer to the black hole.

Appendix A: Solutions of $\lambda(\alpha, \beta)$ and $\eta(\alpha, \beta)$

Given a screen position (α, β) , the corresponding parameters λ, η of null geodesics is determined by Eq. (20). Substituting Eq. (7) into Eq. (20), we have

$$\beta(\lambda, \eta) = \pm_y r \frac{\sqrt{g_{rr}} \Delta_r}{\sqrt{g_{\theta\theta}} \Delta_\theta} \sqrt{\frac{-\Xi^2(\lambda \csc \theta - a \sin \theta)^2 + (\eta + (a - \lambda)^2 \Xi^2) \Delta_\theta}{\Xi^2 (r^2 + a^2 - a\lambda)^2 - \Delta_r (\eta + \Xi^2(\lambda - a)^2)}}, \quad (\text{A1})$$

$$\alpha(\lambda, \eta) = r \frac{\sqrt{g_{rr}}}{\sqrt{g_{\phi\phi}}} \Delta_r \frac{\lambda}{\sqrt{\Xi^2 (r^2 + a^2 - a\lambda)^2 - \Delta_r (\eta + \Xi^2(\lambda - a)^2)}}. \quad (\text{A2})$$

Combining Eq. (A2) and Eq. (A1), we get a quadratic equation of λ :

$$A\lambda^2 + B\lambda + C = 0, \quad (\text{A3})$$

where

$$A = \Xi^2 r^2 \left(\csc^2 \theta \frac{\Delta_r}{\Delta_\theta} - a^2 \Xi^2 + \frac{(\beta^2 + r^2) \Sigma^2 \csc^4 \theta \Delta_r}{\alpha^2 \left((a^2 + r^2)^2 \Delta_\theta^2 \csc^2 \theta - a^2 \Delta_r \right)} \right), \quad (\text{A4})$$

$$B = 2ar^2 \Xi^2 \left(\Xi^2 (a^2 + r^2) - \frac{\Delta_r}{\Delta_\theta} \right), \quad (\text{A5})$$

$$C = \Xi^2 r^2 \left(a^2 \sin^2 \theta \frac{\Delta_r}{\Delta_\theta} - \Xi^2 (a^2 + r^2)^2 \right). \quad (\text{A6})$$

Solving Eq. (A3) and Eq. (A1), and then discarding the irrational solution, we finally obtain

$$\lambda(\alpha, \beta) = -\beth - \sqrt{\beth^2 - \frac{a^2 \sin^2 \theta \Delta_r - \Xi^2 (a^2 + r^2)^2 \Delta_\theta}{\frac{(\beta^2 + r^2) \Sigma^2 \Delta_\theta \csc^4 \theta \Delta_r}{\alpha^2 [(a^2 + r^2)^2 \Delta_\theta^2 \csc^2 \theta - a^2 \Delta_r]} - a^2 \Xi^2 \Delta_\theta + \csc^2 \theta \Delta_r}}, \quad (\text{A7})$$

$$\eta(\alpha, \beta) = -\frac{\lambda^2 \Xi^2 r^2 \Sigma^2 \csc^4 \theta}{\alpha^2 [(a^2 + r^2)^2 \Delta_\theta^2 \csc^2 \theta - a^2 \Delta_r]} + \frac{\Xi^4 (a^2 - a\lambda + r^2)^2}{\Delta_r} - \Xi^4 (a - \lambda)^2, \quad (\text{A8})$$

where

$$\beth = \frac{a (\Xi^2 (a^2 + r^2) \Delta_\theta - \Delta_r)}{\frac{(\beta^2 + r^2) \Sigma^2 \Delta_\theta \csc^4 \theta \Delta_r}{\alpha^2 [(a^2 + r^2)^2 \Delta_\theta^2 \csc^2 \theta - a^2 \Delta_r]} - a^2 \Xi^2 \Delta_\theta + \csc^2 \theta \Delta_r}. \quad (\text{A9})$$

In the limit $\Lambda \rightarrow 0$ of Kerr black holes, Eq. (A7) and Eq. (A8) reduce to the null geodesic parameters related to the ZAMO's screen position in Kerr spacetimes. In the limit of $\Lambda \rightarrow 0$ and $r \rightarrow \infty$, we return to the case of considering distant observers in Kerr spacetimes. The Eq. (A7) and Eq. (A8) reduce to

$$\lambda(\alpha, \beta) = -\alpha \sin \theta, \quad (\text{A10})$$

$$\eta(\alpha, \beta) = (\alpha^2 - a^2) \cos \theta + \beta^2, \quad (\text{A11})$$

which coincide with Eq.(58) and Eq.(59) of [37] (see also [80]).

Appendix B: Redshift factor

In the previous section (section IIC), we presented the equatorial accretion model and provided the four-velocity equation for particles at each equatorial radius. In this appendix, we derive the redshift factor as defined in Eq. (22).

For $r_{\text{ISCO}} < r < r_{\text{OSCO}}$, particles within the accretion disk follow circular orbits, and their corresponding four-velocity is given by Eq. (13). The associated redshift factor is calculated as follows:

$$\begin{aligned} g_{\text{circular}}(\lambda, \eta, r) &= \frac{\nu_{\text{obs}}}{\nu_{\text{em}}} = \frac{k_\mu u_{\text{obs}}^\mu}{k_\mu u_{\text{em}}^\mu} = \frac{-\zeta + \gamma\lambda}{-u^t + \lambda u^\phi} \\ &= \frac{(\gamma\lambda - \zeta) \pm \sqrt{\left(-ya^2 \mp 2a\sqrt{\frac{1}{r^3} - y}\right) - \frac{3}{r} + 1}}{\Xi \left(\left(a\sqrt{\frac{1}{r^3} - y} \pm \lambda\sqrt{\frac{1}{r^3} - y} \right) \mp 1 \right)}, \end{aligned} \quad (\text{B1})$$

where ζ and γ are defined in Eq. (16):

$$\zeta = 2\sqrt{\frac{\Xi^2 \Sigma \left((a^2 + r^2)^2 \Delta_\theta^2 - a^2 \sin^2 \theta \Delta_r \right)}{\Delta_\theta \Delta_r (a^2 \cos(2\theta) + a^2 + 2r^2)^2}} \Bigg|_{(r_0, \theta_0)}, \quad (\text{B2})$$

$$\gamma = \frac{\zeta (a ((a^2 + r^2) \Delta_\theta - \Delta_r))}{(a^2 + r^2)^2 \Delta_\theta^2 - a^2 \sin^2 \theta \Delta_r} \Bigg|_{(r_0, \theta_0)}. \quad (\text{B3})$$

For $r_H < r < r_{\text{ISCO}}$, the redshift factor is

$$g_{\text{infall}}(r, \lambda, \eta, \nu_r) = \frac{-\zeta + \gamma\lambda}{-u_s^r + \nu_r \frac{\sqrt{R(r)}}{\Delta_r} u_s^r + \lambda u_s^\phi}, \quad \nu_r = \text{Sign}[P_r], \quad (\text{B4})$$

where

$$u_s^t = -g^{00} E_{\text{ISCO}} + g^{03} L_{\text{ISCO}}, \quad u_s^\phi = -g^{03} E_{\text{ISCO}} + g^{33} L_{\text{ISCO}}, \quad (\text{B5})$$

$$u_s^r = -\sqrt{g^{11} (-E_{\text{ISCO}}^2 g^{00} + 2E_{\text{ISCO}} L_{\text{ISCO}} g^{03} - L_{\text{ISCO}}^2 g^{33} - 1)}. \quad (\text{B6})$$

Appendix C: null bound geodesic condition

Solving the circular orbit conditions $\dot{r} = \ddot{r} = 0$ in Kerr-de sitter spacetimes, we find that

$$\begin{aligned}\lambda(R) &= \frac{-4r\Delta_r}{a\Delta'_r} + \frac{r^2 + a^2}{a} \Big|_{r=R}, \\ \eta(R) &= \frac{16r^2\Xi^2\Delta_r}{(\Delta'_r)^2} - \Xi^2(\lambda - a)^2 \Big|_{r=R},\end{aligned}\tag{C1}$$

where R is the radii of bound orbits. The range of R is determined by an inequality $\Theta(\theta) \geq 0$ and a implied condition $r_+ < R < r_C$. Using Eq. (C1), the condition $\Theta(\theta) \geq 0$ becomes

$$16r^2a^2\sin^2\theta\Delta_\theta\Delta_r \geq (4r\Delta_r - \Sigma\Delta'_r)^2 \Big|_{r=R},\tag{C2}$$

or

$$R \in [r_+^\gamma, r_-^\gamma],\tag{C3}$$

where r_\pm^γ is the roots of $\eta = 0$ in the range $r_+ < r < r_C$:

$$r_\pm^\gamma = k[1 + \sqrt{1 - 4a^2\Lambda} \cos(\frac{1}{3} \arccos(\frac{\mp|b|}{9M^2}))],\tag{C4}$$

$$k = \frac{6M}{3 + 4a^2\Lambda}, \quad b = \frac{9M^2 - 32a^6\Lambda^2 - 48a^4\Lambda + 18a^2(6\Lambda M^2 - 1)}{9M^2(4a^2\Lambda - 1)\sqrt{1 - 4a^2\Lambda}}.\tag{C5}$$

-
- [1] Kazunori Akiyama et al. First M87 Event Horizon Telescope Results. I. The Shadow of the Supermassive Black Hole. *Astrophys. J. Lett.*, 875:L1, 2019.
 - [2] Kazunori Akiyama et al. First M87 Event Horizon Telescope Results. II. Array and Instrumentation. *Astrophys. J. Lett.*, 875(1):L2, 2019.
 - [3] Kazunori Akiyama et al. First M87 Event Horizon Telescope Results. III. Data Processing and Calibration. *Astrophys. J. Lett.*, 875(1):L3, 2019.
 - [4] Kazunori Akiyama et al. First M87 Event Horizon Telescope Results. IV. Imaging the Central Supermassive Black Hole. *Astrophys. J. Lett.*, 875(1):L4, 2019.
 - [5] Kazunori Akiyama et al. First M87 Event Horizon Telescope Results. V. Physical Origin of the Asymmetric Ring. *Astrophys. J. Lett.*, 875(1):L5, 2019.
 - [6] Kazunori Akiyama et al. First M87 Event Horizon Telescope Results. VI. The Shadow and Mass of the Central Black Hole. *Astrophys. J. Lett.*, 875(1):L6, 2019.
 - [7] Ru-Sen Lu, Keiichi Asada, Thomas P. Krichbaum, et al. A ring-like accretion structure in m87 connecting its black hole and jet. *Nature*, 616(7958):686–690, 2023.
 - [8] J. L. Synge. The escape of photons from gravitationally intense stars. *Monthly Notices of the Royal Astronomical Society*, 131(3):463–466, 1966.
 - [9] James M. Bardeen. Timelike and null geodesics in the kerr metric. *Black holes (Les astres occlus)*, pages 215 – 239, 1973.
 - [10] Volker Perlick and Oleg Yu Tsupko. Calculating black hole shadows: Review of analytical studies. *Physics Reports*, 947:1–39, 2022.
 - [11] Pedro V. P. Cunha, Carlos A. R. Herdeiro, Eugen Radu, and Helgi F. Runarsson. Shadows of kerr black holes with and without scalar hair. *International Journal of Modern Physics D*, 25(9):1641021, 2016.
 - [12] Ramesh Narayan, Michael D. Johnson, and Charles F. Gammie. The shadow of a spherically accreting black hole. *The Astrophysical Journal*, 885(2):L33, 2019.
 - [13] Volker Perlick, Oleg Yu Tsupko, and Gennady S. Bisnovatyi-Kogan. Black hole shadow in an expanding universe with a cosmological constant. *Physical Review D*, 97(10):104062, 2018.
 - [14] Hui-Min Wang, Yu-Meng Xu, and Shao-Wen Wei. Shadows of kerr-like black holes in a modified gravity theory. *J. Cosmol. Astropart. Phys.*, 2019(3):046–046, 2019.
 - [15] Yang Huang, Yi-Ping Dong, and Dao-Jun Liu. Revisiting the shadow of a black hole in the presence of a plasma. *International Journal of Modern Physics D*, 27(12):1850114, 2018.
 - [16] Ahmadjon Abdujabbarov, Muhammed Amir, Bobomurat Ahmedov, and Sushant G. Ghosh. Shadow of rotating regular black holes. *Physical Review D*, 93(10):104004, 2016.
 - [17] Zilong Li and Cosimo Bambi. Measuring the Kerr spin parameter of regular black holes from their shadow. *JCAP*, 01:041, 2014.

- [18] Ahmadjon Abdujabbarov, Farruh Atamurotov, Yusuf Kucukakca, Bobomurat Ahmedov, and Ugur Camci. Shadow of Kerr-Taub-NUT black hole. *Astrophys. Space Sci.*, 344:429–435, 2013.
- [19] Akifumi Yumoto, Daisuke Nitta, Takeshi Chiba, and Naoshi Sugiyama. Shadows of Multi-Black Holes: Analytic Exploration. *Phys. Rev. D*, 86:103001, 2012.
- [20] Jason Dexter and P. Chris Fragile. Tilted black hole accretion disc models of Sagittarius A*: time-variable millimetre to near-infrared emission. *Mon. Not. Roy. Astron. Soc.*, 432:2252, 2013.
- [21] Leonardo Amarilla, Ernesto F. Eiroa, and Gaston Giribet. Null geodesics and shadow of a rotating black hole in extended Chern-Simons modified gravity. *Phys. Rev. D*, 81:124045, 2010.
- [22] Cosimo Bambi and Naoki Yoshida. Shape and position of the shadow in the $\delta = 2$ Tomimatsu-Sato space-time. *Class. Quant. Grav.*, 27:205006, 2010.
- [23] Lei Huang, Mike Cai, Zhi-Qiang Shen, and Feng Yuan. Black Hole Shadow Image and Visibility Analysis of Sagittarius A*. *Mon. Not. Roy. Astron. Soc.*, 379:833–840, 2007.
- [24] Heino Falcke, Fulvio Melia, and Eric Agol. Viewing the shadow of the black hole at the galactic center. *Astrophys. J. Lett.*, 528:L13, 2000.
- [25] Pedro V. P. Cunha, Carlos A. R. Herdeiro, and Eugen Radu. Fundamental photon orbits: black hole shadows and spacetime instabilities. *Phys. Rev. D*, 96(2):024039, 2017.
- [26] Ahmadjon Abdujabbarov, Muhammed Amir, Bobomurat Ahmedov, and Sushant G. Ghosh. Shadow of rotating regular black holes. *Phys. Rev. D*, 93(10):104004, 2016.
- [27] Ming Zhang and Minyong Guo. Can shadows reflect phase structures of black holes? *Eur. Phys. J. C*, 80(8):790, 2020.
- [28] Minyong Guo and Peng-Cheng Li. Innermost stable circular orbit and shadow of the 4D Einstein–Gauss–Bonnet black hole. *Eur. Phys. J. C*, 80(6):588, 2020.
- [29] Zezhou Hu, Zhen Zhong, Peng-Cheng Li, Minyong Guo, and Bin Chen. QED effect on a black hole shadow. *Phys. Rev. D*, 103(4):044057, 2021.
- [30] Yehui Hou, Minyong Guo, and Bin Chen. Revisiting the shadow of braneworld black holes. *Phys. Rev. D*, 104(2):024001, 2021.
- [31] Mingzhi Wang, Songbai Chen, and Jiliang Jing. Kerr black hole shadows in Melvin magnetic field with stable photon orbits. *Phys. Rev. D*, 104(8):084021, 2021.
- [32] Qingyu Gan, Peng Wang, Houwen Wu, and Haitang Yang. Photon ring and observational appearance of a hairy black hole. *Phys. Rev. D*, 104(4):044049, 2021.
- [33] Yuan Meng, Xiao-Mei Kuang, and Zi-Yu Tang. Photon regions, shadow observables, and constraints from M87* of a charged rotating black hole. *Phys. Rev. D*, 106(6):064006, 2022.
- [34] Jinsong Yang, Cong Zhang, and Yongge Ma. Shadow and stability of quantum-corrected black holes. *Eur. Phys. J. C*, 83(7):619, 2023.
- [35] F. H. Vincent, S. E. Gralla, A. Lupsasca, and M. Wielgus. Images and photon ring signatures of thick disks around black holes. *Astronomy & Astrophysics*, 667:A170, 2022.
- [36] Thomas Bronzwaer and Heino Falcke. The Nature of Black Hole Shadows. *Astrophys. J.*, 920(2):155, 2021.
- [37] Samuel E. Gralla and Alexandru Lupsasca. Lensing by kerr black holes. *Physical Review D*, 101(4):044031, 2020.
- [38] J.F Plebanski and M Demianski. Rotating, charged, and uniformly accelerating mass in general relativity. *Annals of Physics*, 98(1):98–127, 1976.
- [39] J. B. Griffiths and J. Podolsky. A new look at the plebanski-demianski family of solutions. *Int. J. Mod. Phys. D*, 15(3):335–369, 2006.
- [40] Arne Grenzebach, Volker Perlick, and Claus Lämmerzahl. Photon regions and shadows of kerr-newman-NUT black holes with a cosmological constant. *Physical Review D*, 89(12):124004, 2014.
- [41] Arne Grenzebach, Volker Perlick, and Claus Lämmerzahl. Photon Regions and Shadows of Accelerated Black Holes. *Int. J. Mod. Phys. D*, 24(09):1542024, 2015.
- [42] J. P. Luminet. Image of a spherical black hole with thin accretion disk. *Astronomy and Astrophysics*, 75:228–235, 1979.
- [43] Michael D. Johnson et al. Universal interferometric signatures of a black hole’s photon ring. *Sci. Adv.*, 6(12):eaaz1310, 2020.
- [44] Andrew Chael, Michael D. Johnson, and Alexandru Lupsasca. Observing the inner shadow of a black hole: A direct view of the event horizon. *The Astrophysical Journal*, 918(1):6, 2021.
- [45] Roman Gold. Verification of radiative transfer schemes for the EHT. *The Astrophysical Journal*, 2020.
- [46] Lia Medeiros, Dimitrios Psaltis, Tod R. Lauer, and Feryal Özel. The Image of the M87 Black Hole Reconstructed with PRIMO. *Astrophys. J. Lett.*, 947(1):L7, 2023.
- [47] Cong Zhang, Yongge Ma, and Jinsong Yang. Black hole image encoding quantum gravity information. *Phys. Rev. D*, 108(10):104004, 2023.
- [48] Xin Qin, Songbai Chen, Zelin Zhang, and Jiliang Jing. Polarized image of a rotating black hole surrounded by a cold dark matter halo. *Eur. Phys. J. C*, 83(2):159, 2023.
- [49] Mingzhi Wang, Songbai Chen, and Jiliang Jing. Determination of the spin parameter and the inclination angle from the primary and secondary images caused by gravitational lensing. *Sci. China Phys. Mech. Astron.*, 66(11):110411, 2023.
- [50] Reggie C. Pantig, Ali Övgün, and Durmuş Demir. Testing symmergent gravity through the shadow image and weak field photon deflection by a rotating black hole using the M87* and Sgr. A* results. *Eur. Phys. J. C*, 83(3):250, 2023.
- [51] Rajibul Shaikh. Testing black hole mimickers with the Event Horizon Telescope image of Sagittarius A*. *Mon. Not. Roy. Astron. Soc.*, 523(1):375–384, 2023.

- [52] Xin Qin, Songbai Chen, Zelin Zhang, and Jiliang Jing. Polarized Image of a Rotating Black Hole in Scalar–Tensor–Vector–Gravity Theory. *Astrophys. J.*, 938(1):2, 2022.
- [53] Yehui Hou, Zhenyu Zhang, Haopeng Yan, Minyong Guo, and Bin Chen. Image of a Kerr-Melvin black hole with a thin accretion disk. *Phys. Rev. D*, 106(6):064058, 2022.
- [54] Qingyu Gan, Peng Wang, Houwen Wu, and Haitang Yang. Photon spheres and spherical accretion image of a hairy black hole. *Phys. Rev. D*, 104(2):024003, 2021.
- [55] Mehrab Momennia, Alfredo Herrera-Aguilar, and Ulises Nucamendi. Kerr black hole in de sitter spacetime and observational redshift: Toward a new method to measure the hubble constant. *Phys. Rev. D*, 107:104041, May 2023.
- [56] Kenta Hioki and Kei-ichi Maeda. Measurement of the Kerr Spin Parameter by Observation of a Compact Object’s Shadow. *Phys. Rev. D*, 80:024042, 2009.
- [57] Naoki Tsukamoto, Zilong Li, and Cosimo Bambi. Constraining the spin and the deformation parameters from the black hole shadow. *JCAP*, 06:043, 2014.
- [58] Naoki Tsukamoto. Black hole shadow in an asymptotically-flat, stationary, and axisymmetric spacetime: The Kerr-Newman and rotating regular black holes. *Phys. Rev. D*, 97(6):064021, 2018.
- [59] Zhi-Shuo Qu, Towe Wang, and Chao-Jun Feng. Reduced Kiselev black hole. *Eur. Phys. J. C*, 83(9):784, 2023.
- [60] Zhi-Shuo Qu, Towe Wang, and Chao-Jun Feng. Images of nonsingular nonrotating black holes in conformal gravity. *arXiv:2301.07326*, 2023.
- [61] Mingzhi Wang, Songbai Chen, and Jiliang Jing. Chaotic shadows of black holes: a short review. *Commun. Theor. Phys.*, 74(9):097401, 2022.
- [62] Volker Perlick and Oleg Yu. Tsupko. Calculating black hole shadows: Review of analytical studies. *Phys. Rept.*, 947:1–39, 2022.
- [63] Songbai Chen, Jiliang Jing, Wei-Liang Qian, and Bin Wang. Black hole images: A review. *Sci. China Phys. Mech. Astron.*, 66(6):260401, 2023.
- [64] Samuel E. Gralla, Daniel E. Holz, and Robert M. Wald. Black hole shadows, photon rings, and lensing rings. *Physical Review D*, 100(2):024018, 2019.
- [65] Adam G. Riess et al. Observational evidence from supernovae for an accelerating universe and a cosmological constant. *Astron. J.*, 116:1009–1038, 1998.
- [66] B. Carter. Black holes equilibrium states. In *Les Houches Summer School of Theoretical Physics: Black Holes*, pages 57–214, 1973.
- [67] Peng-Cheng Li, Minyong Guo, and Bin Chen. Shadow of a spinning black hole in an expanding universe. *Physical Review D*, 101(8):084041, 2020.
- [68] Eunice Omwoyo, Humberto Belich, Júlio C. Fabris, and Hermano Velten. Remarks on the black hole shadows in kerr-de sitter space times. *Eur. Phys. J. C*, 82(5):395, 2022.
- [69] Samuel E. Gralla, Alexandru Lupsasca, and Daniel P. Marrone. The shape of the black hole photon ring: A precise test of strong-field general relativity. *Physical Review D*, 102(12):124004, 2020.
- [70] Zdeněk Stuchlík and Petr Slaný. Equatorial circular orbits in the kerr–de sitter spacetimes. *Physical Review D*, 69(6):064001, 2004.
- [71] James M. Bardeen, William H. Press, and Saul A. Teukolsky. Rotating black holes: Locally nonrotating frames, energy extraction, and scalar synchrotron radiation. *The Astrophysical Journal*, 178:347, 1972.
- [72] Sarp Akcay and Richard Matzner. Kerr-de sitter universe. *Class. Quantum Grav.*, 28(8):085012, 2011.
- [73] Marek A. Abramowicz and P. Chris Fragile. Foundations of black hole accretion disk theory. *Living Reviews in Relativity*, 16(1):1, 2013.
- [74] M. Jaroszynski and A. Kurpiewski. Optics near kerr black holes: spectra of advection dominated accretion flows. *Astron. Astrophys.*, 326:419, 1997.
- [75] Yehui Hou, Zhenyu Zhang, Haopeng Yan, Minyong Guo, and Bin Chen. Image of kerr-melvin black hole with thin accretion disk. *Physical Review D*, 106(6):064058, 2022.
- [76] Samuel E. Gralla and Alexandru Lupsasca. Null geodesics of the kerr exterior. *Physical Review D*, 101(4):044032, 2020.
- [77] Eunice Omwoyo, Humberto Belich, Júlio C. Fabris, and Hermano Velten. Black hole lensing in Kerr-de Sitter spacetimes. *Eur. Phys. J. Plus*, 138(11):1043, 2023.
- [78] Yasushi Mino. Perturbative approach to an orbital evolution around a supermassive black hole. *Physical Review D*, 67(8):084027, 2003.
- [79] Milton Abramowitz and Irene A Stegun. *Handbook of mathematical functions with formulas, graphs, and mathematical tables*, volume 55. US Government printing office, 1948.
- [80] Samuel E Gralla, Alexandru Lupsasca, and Andrew Strominger. Observational signature of high spin at the event horizon telescope. *Monthly Notices of the Royal Astronomical Society*, 475(3):3829–3853, 2018.